Journal of Materials Chemistry A

ROYAL SOCIETY OF CHEMISTRY

PAPER

View Article Online
View Journal | View Issue

Cite this: J. Mater. Chem. A, 2024, 12, 7122

One-dimensional van der Waals transition metal chalcogenide as an anode material for advanced lithium-ion batteries†

Woosung Choi,‡[a] Seungbae Oh,‡[b] Sunhyun Hwang,‡[a] Sudong Chae,[b] Hyunyoung Park,[a] Wontae Lee,[a] Chaeheon Woo,[b] Xue Dong,[e] Kyung Hwan Choi,[e] Jungyoon Ahn,[b] Yeongjin Kim,[b] Xiaojie Zhang,[b] Jinsu Kang,[b] Hyeon-Seok Bang,[b] Jiho Jeon,[e] Hyung-Suk Oh,[cd] Jongsoon Kim,[af] Jae-Young Choi *[bce] and Won-Sub Yoon *[af]

Received 8th November 2023
Accepted 3rd January 2024

DOI: 10.1039/d3ta06867f

rsc.li/materials-a

In response to the swiftly growing demand for batteries in the electric vehicle sector, it is necessary to develop novel anode materials with elevated energy and power density. As an alternative to conventional graphite anodes, conversion-based transition metal chalcogenide materials were proposed. However, the tremendous volume expansion and the poor kinetics associated with conversion-based transition metal chalcogenide electrodes limit their further application. In this study, we explore the application of one-dimensional van der Waals (1D vdW) Nb_2Se_9 as an anode material for Li-ion batteries (LIBs). The Nb_2Se_9 electrode, when tested at a current rate of 0.1 A g^{-1} over 100 cycles, exhibits a substantial reversible specific capacity of 542.2 mA h g^{-1}. Even when subjected to a current density of 3.2 A g^{-1}, it maintains a high capacity of 272.0 mA h g^{-1}. Combined results of synchrotron X-ray absorption spectroscopy and scanning electron microscopy show that the one-dimensional Nb_2Se_9 phase is maintained after the accommodation of lithium ions. This result can be explained by the unique 1D vdW structure, which provides a short diffusion length and ample space to handle the volume expansion. Additionally, the substantial electron cloud of Se surrounding the Nb–Nb framework acts as a Se–Se buffer layer, protecting the one-dimensional structure. Therefore, Li ions can react with the externally exposed Se–Se buffer layer to form dispersed fragments, leading to superior structural stability. These results will not only enhance our understanding of the reaction mechanism within Nb_2Se_9 materials but also promote the potential utilization of 1D vdW materials as advanced electrode materials for Li-ion batteries.

Introduction

The efforts to reduce the emission of greenhouse gases resulting from the utility of fossil fuels are driving the promotion of electric transportation systems, encompassing hybrid electric vehicles and fully electric vehicles. To meet these industrial needs, advanced lithium-ion battery (LIB) active materials with high capacity and power density are necessary. Over the past decade, significant developments have been achieved in cathode materials, and several options, such as $LiCoO_2$, $LiMnO_2$, $LiFePO_4$, and $LiNi_{1-x-y}Mn_xCo_yO_2$, have approached commercial viability. However, when considering anode materials, only graphite has been the exclusive choice, as it was introduced to the market by SONY in 1991.[1] Although graphite is a successful material for LIB anodes because of its low average voltage, low cost, and abundant raw materials, the insufficient specific capacity of 372 mA h g^{-1} requires novel chemistry establishing advanced lithium storage processes that are not limited by intercalation.[2]

Hence, in recent decades, various anode materials have garnered significant interest as potential substitutes for conventional graphite anodes in commercial applications. These materials cover Li-alloying materials (Si,[3,4] Ge,[5] Sn,[6]

[a]Department of Energy Science, Sungkyunkwan University, Suwon 16419, Republic of Korea. E-mail: wsyoon@skku.edu

[b]School of Advanced Materials Science & Engineering, Sungkyunkwan University, Suwon 16419, Republic of Korea. E-mail: jy.choi@skku.edu

[c]School of Advanced Materials Science & Engineering and KIST-SKKU Carbon-Neutral Research Center, Sungkyunkwan University, Suwon 16419, Republic of Korea

[d]Clean Energy Research Center, Korea Institute of Science and Technology (KIST), Seoul 02792, Republic of Korea

[e]SKKU Advanced Institute of Nanotechnology (SAINT), Sungkyunkwan University, Suwon 16419, Republic of Korea

[f]SKKU Institute of Energy Science and Technology (SIEST), Sungkyunkwan University, Suwon 16419, Republic of Korea

† Electronic supplementary information (ESI) available. See DOI: https://doi.org/10.1039/d3ta06867f

‡ These authors contributed equally.

SnO_2,[7] *etc.*) and conversion-based transition metal chalcogenides (MnO_2,[8,9] Co_3O_4,[10,11] Fe_2O_3,[12] MoS_2,[13] WS_2,[14] *etc*). Extensively investigated for their remarkable average specific capacity of approximately 2000 mA h g^{-1}, Li-alloying materials have received significant interest as prospective anode materials for advanced lithium-ion batteries (LIBs). Nonetheless, the extreme volume change that occurs during the generation of the Li-alloy phase by the breaking of bonds between host atoms generally results in rapid capacity degradation.[15] Since the first demonstration of lithium storage *via* the conversion mechanism in 2000,[16] transition metal chalcogenides (-oxides, -sulfides, and -selenides) have been regarded as attractive candidates because of their distinctive electrochemical reaction pathway and high initial coulombic efficiency.[17] However, such metal chalcogenides are still facing challenges in terms of poor kinetics due to their relatively low intrinsic electrical conductivity and unfavorable mechanical fracture/decrepitation of particles caused by volume expansion upon lithium accommodation.[18,19]

Accordingly, the one-dimensional van der Waals (1D vdW) material Nb_2Se_9 could be considered an alternative for high-capacity and high-stability electrodes. The 1D molecular structure of Nb_2Se_9 with strong covalent bonds between center atoms and vdW interaction between chain structures shows many advantages for the LIB anode material. (i) Surface-exposed Se atoms increase the possibility of reaction with Li^+ during an electrochemical process, which can improve the rate capability.[20,21] (ii) A one-dimensional structure enables the absorption of the strain caused by lithium insertion and removal in a particular direction, and the internal space between chains can serve as a structural buffer, preventing the clustering of active materials and structural collapse.[19,22] (iii) The absence of dangling bonds that induce unwanted side reactions with the electrolyte mitigates capacity degradation and provides superior cycling performance.[23,24] (iv) High theoretical capacity is expected, assuming a complete conversion reaction with a number of lithium-active chalcogenide elements compared with a 2D or 3D material.[20] Since D. W. Murphy's first report of the electrochemical lithiation of Nb_2Se_9 published in 1977,[25] although 1D vdW Nb_2Se_9 was utilized in energy applications such as electrocatalysts,[26] their utilization as an anode material for LIBs has received restricted interest. In 2021, Wu *et al.*[27] utilized flower-like Nb_2Se_9 (F-Nb_2Se_9) and polycrystalline rod-like Nb_2Se_9 (R-Nb_2Se_9) as anode materials and considered the lithium storage mechanism of Nb_2Se_9 as the conversion reaction through *ex situ* X-ray diffraction (XRD) analysis. However, given the ambiguity of diffraction patterns in the conversion reaction, *in situ* XRD analysis must be performed along with various analyses, such as spectroscopic analysis, to confirm the conversion reaction.

Multiple characterization techniques, including *in situ* XRD, X-ray absorption spectroscopy (XAS), transmission electron microscopy (TEM), and scanning electron microscopy (SEM) were adopted to examine the electrochemical and structural behavior of Nb_2Se_9. The results of the electrochemical experiments show that single-crystalline Nb_2Se_9 exhibited an improved rate capability compared to the previously reported R-Nb_2Se_9. This result can be due to the advantages of single-crystalline 1D materials with a short lithium diffusion length and high surface area. In addition, *in situ* XRD and XAS analyses demonstrate that the lithium storage process occurs through the conversion reaction by the detection of Li_2Se. SEM data also corroborate the superior structural stability of single-crystalline Nb_2Se_9, demonstrating the unchanged crystal morphology. This finding will provide valuable perspectives for the advancement of high-performance 1D electrode materials for LIBs.

Experimental

Material preparation

Niobium selenide (Nb_2Se_9) was prepared by a solid-state reaction using Nb (powder, 99.99%, −325 mesh, Alfa Aesar) and Se (powder, 99+%, Alfa Aesar) elemental powders. The starting materials, 2.5 mmol of Nb and 22.5 mmol of Se powder, were uniformly mixed in a mortar. The powder mixture was pelletized and sealed in a 10 cm-long quartz tube. The quartz tube was evacuated and heated to 600 °C (2.3 °C min^{-1}) for 72 h and then cooled down (at 10 °C h^{-1}) in a box furnace. The product was a dark gray powder. The unreacted Se was removed in a furnace under an argon atmosphere at 250 °C for a duration of 24 hours.

Electrode fabrication and electrochemical tests

The prepared Nb_2Se_9 was mixed with polyamide imide (Torlon 4000 T, Solvay) binder and a CNT (CAS No. 308068-56-6, Aldrich) conductive agent in a weight ratio of 60 : 20 : 20 and then placed on Cu foil and coated by using a doctor blade. The coated electrode was dried at 120 °C for 5 h under vacuum. 12 mm diameter disks were cut from the electrode, and coin-type cells (CR2032) were assembled in a dry room. The cell components included a Celgard 3501 separator, an electrolyte consisting of 1.3 M $LiPF_6$ in a 3 : 7 volume ratio mixture of ethylene carbonate (EC) and diethyl carbonate (DEC), and Li foil as the counter electrode. Galvanostatic measurement was performed in the voltage range of 0.001–3.0 V (*vs.* Li/Li^+) by using a BaSyTec (CTS-Lab, Germany) battery cycler. Cyclic voltammetry (CV) data were acquired using a potentiostat analyzer (BioLogic, VMP3).

Material characterization

The morphologies of the samples were investigated by using a scanning electron microscope (SEM, JSM-7500F, and JSM-IT800, Japan) and transmission electron microscope (TEM, JEM-2100F, Japan). Annular dark-field scanning transmission electron microscopy (ADF STEM) was performed by using an aberration-corrected scanning transmission electron microscope (STEM, JEM ARM 200F, Japan).

Synchrotron-based X-ray analysis

High-resolution powder diffraction (HRPD) patterns were obtained at the 9B HRPD beamline at Pohang Light Source-II (PLS-II). The pristine Nb_2Se_9 powder was subjected to scanning in the range of 10° to 130.5° with a 0.01° step size. The lattice parameters were acquired through Rietveld refinement of the collected HRPD patterns using the GSAS-II software package.[28]

During the first two cycles, *in situ* XRD measurement was performed at the 9A U-SAXS beamline at Pohang Light Source-II (PLS-II) with a wavelength of 0.61899 Å. For the *in situ* experiment, a coin cell was designed to allow X-ray penetration, and during the electrochemical measurement, the test was conducted in the voltage range of 0.001–3.0 V (*vs.* Li/Li^+) at a constant current rate of 0.1 A g^{-1}. 2θ angles from the acquired patterns were transformed to their corresponding angles with a Cu Kα source. *Ex situ* XAS data were collected at the 10C-wide XAFS beamline at PLS-II. Nb and Se K-edge spectra were measured in the fluorescence mode and detuned to 70–80% of their original intensity to minimize high-order harmonics. The storage ring ran at 3.0 GeV with a ring current of 300 mA. Energy calibration was performed by exploiting the first inflection point of Nb and Se metal spectra as a reference (Nb K-edge = 18 986 eV and Se K-edge = 12 658 eV). The reference spectra of Nb and Se were collected at the same time, measuring the spectra of *ex situ* samples.

Computational details

The Vienna *ab initio* simulation package (VASP) was utilized for conducting all density functional theory (DFT) calculations.[29] In the VASP, projector-augmented wave (PAW) pseudopotentials[30] were applied, along with a plane-wave basis set. The Perdew–Burke–Ernzerhof (PBE) parametrization of the generalized gradient approximation (GGA)[31] was used for the exchange–correlation function. DFT calculations utilized a 5 × 5 × 4 *k*-point grid for assessing a 1 × 1 × 1 supercell configuration of Nb_2Se_9. All computations employed a kinetic energy cutoff of 500 eV, and structural optimization continued until the force within the unit cell reached a convergence of 0.03 eV $Å^{-1}$. The cluster-assisted statistical mechanics (CASM) software[32] was employed to create Li^+/vacancy arrangements for each composition. Subsequently, complete DFT calculations were performed on up to 20 configurations exhibiting the lowest electrostatic energy for each composition. These configurations were used to determine the convex hull of $Li_xNb_2Se_9$, using the following equation.

$$E_{for} = E(Li_xNb_2Se_9) - \frac{(6-x)E(Li_0Nb_2Se_9) + xE(Li_6Nb_2Se_9)}{6}$$

where E_{for} is the relative formation energy for the most stable configuration of each component.

Results and discussion

The successful synthesis of Nb_2Se_9 was confirmed by using the high-resolution powder diffraction (HRPD) pattern of the prepared material. Fig. 1a displays the recorded and computed HRPD patterns, with all peaks corresponding to a singular-phase triclinic unit cell and $P\bar{1}$ space group, as shown. The lattice parameters are $a = 8.180$ Å, $b = 8.323$ Å, and $c = 13.083$ Å, which agree well with the reported structural details for Nb_2Se_9.[21,33] The SEM and TEM images (Fig. 1b, c, and S1†) confirmed that the rod structure of 1D vdW Nb_2Se_9 has tens of micro-sized lengths and a diameter distribution of 100–500 nm. As presented in the annular dark-field scanning transmission

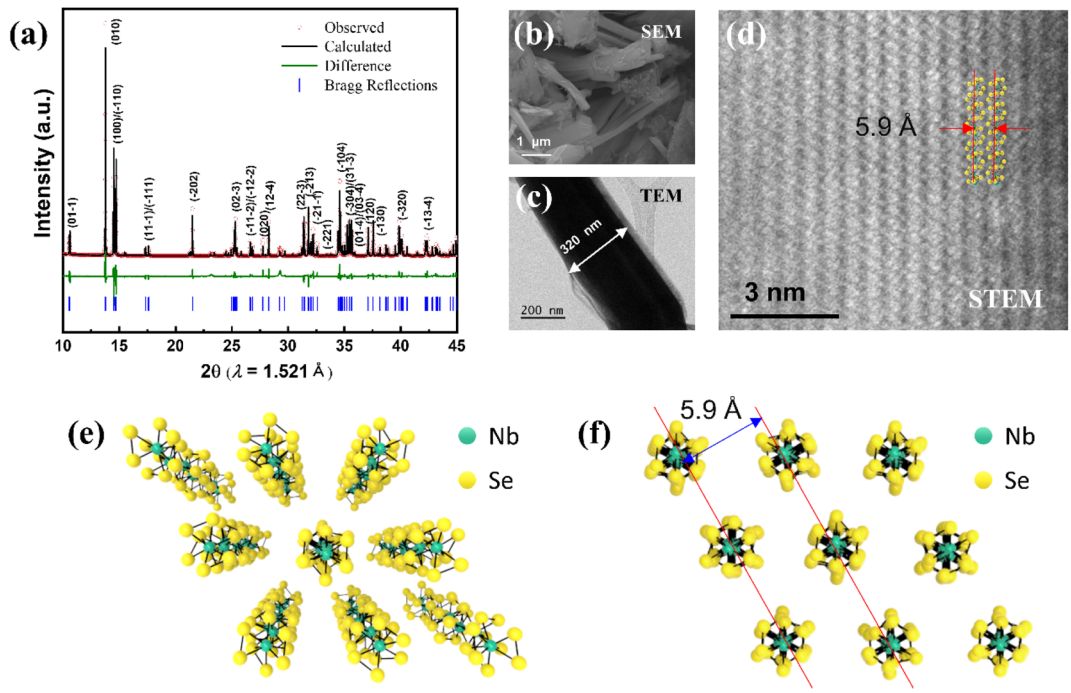

Fig. 1 (a) Observed (red circle) and calculated (solid line) XRD patterns, and difference data (green line) for pristine Nb_2Se_9 powder obtained from Rietveld refinement of HRPD patterns. (b) Low-magnification SEM image and (c) scanning TEM images of the Nb_2Se_9 powder sample. (d) ADF-STEM images demonstrating the chain structure of pristine Nb_2Se_9 with an atomic arrangement. (e) Overall schematic projection of the crystal structure and (f) crystal structure projected along the <111> direction.

electron microscope (ADF-STEM) image in Fig. 1d, the Nb_2Se_9 crystal was composed of molecular unit chains. Given the weak vdW interaction between the unit chains, the *d*-spacing in the (−110) plane, which corresponds to the interchain plane, has a large value of 5.9 Å. The schematic illustration and structural projection of Nb_2Se_9 along the <111> direction are shown in Fig. 1e and f. The structure of the Nb_2Se_9 chain consists of switching tetra-Se (Se_4) and penta-Se (Se_5) groups along linearly connected niobium (Nb) atoms.[21] The Nb–Nb chain surrounded by Se atoms forms a one-dimensional structure, and vdW interactions between each chain has a significant role in maintaining the bundle-sized rod structure. The facilitated Li^+ diffusion path, exposed Se-rich surface, and absence of dangling bonds in the one-dimensional arrangement provide high-rate and high-stability characteristics as an electrode material for LIBs.

In our investigation of the Li storage behavior of 1D vdW Nb_2Se_9 as a LIB anode material, we conducted various electrochemical measurements, as shown in Fig. 2. The voltage profile of the Nb_2Se_9 electrode during the 20 cycles at a current rate of 0.1 A g^{-1} is presented in Fig. 2a. The first discharge and charge processes achieved capacities of 1108.3 and 724.9 mA h g^{-1}, respectively. Following stabilization of the lithium storage reaction by the 20th cycle, a consistent reversible capacity of 545.1 mA h g^{-1} was exhibited, which was maintained until the 100th cycle, demonstrating a capacity of 542.2 mA h g^{-1}. Considering the theoretical limit for storing lithium (Nb_2Se_9 + $18Li^+ + 18e^- \leftrightarrow 2Nb + 9Li_2Se$ or $Li_{18}Nb_2Se_9$: 538 mA h g^{-1}), these results indicate that all Nb_2Se_9 particles possibly contribute to the capacity based on the above equation. In the cyclic voltammetry (CV) profile (Fig. 2b), the cathodic peak at 1.6 V was initially monitored, but this peak vanished in subsequent cycles, and a new peak was observed at 1.8 V, indicating the reduction of overpotential through phase optimization in the initial cathodic scan. Furthermore, the anodic peak at 2.2 V decreases as the cathodic peak at 1.8 V decreases, indicating a correlation between the two reactions. As shown in Fig. S2,† the redox reaction at around 1.7 and 1.9 V during the first and second discharging process as well as at around 1.8 and 2.2 V during the charging process was observed only in the Nb_2Se_9/CNT electrode, meaning that these peaks observed during CV cycling are only related to the redox reactions in Nb_2Se_9. Therefore, the reduction and shift of cathodic and anodic peaks are a consequence of the phase optimization and stabilization of the redox reaction of Nb_2Se_9 for 20 cycles. Based on the Nb-based chalcogenide material, the peak at 1.9 V during the second discharging process corresponds to lithium insertion to the Nb_2Se_9 phase, and the peak at 1.0 V is associated with a conversion reaction, which forms the Nb metal and Li_2Se phase; moreover, the peaks at 1.7 and 2.2 V during the charging process indicate the conversion reaction from Nb and Li_2Se to form $Li_xNb_2Se_9$ and desertion of lithium ions to form Nb_2Se_9 respectively.[27,34–36]

The excellent rate performance of Nb_2Se_9 confirmed that a capacity of 272.0 mA h g^{-1} was maintained even at a high current density of 3.2 A g^{-1}, and the capacity was restored to

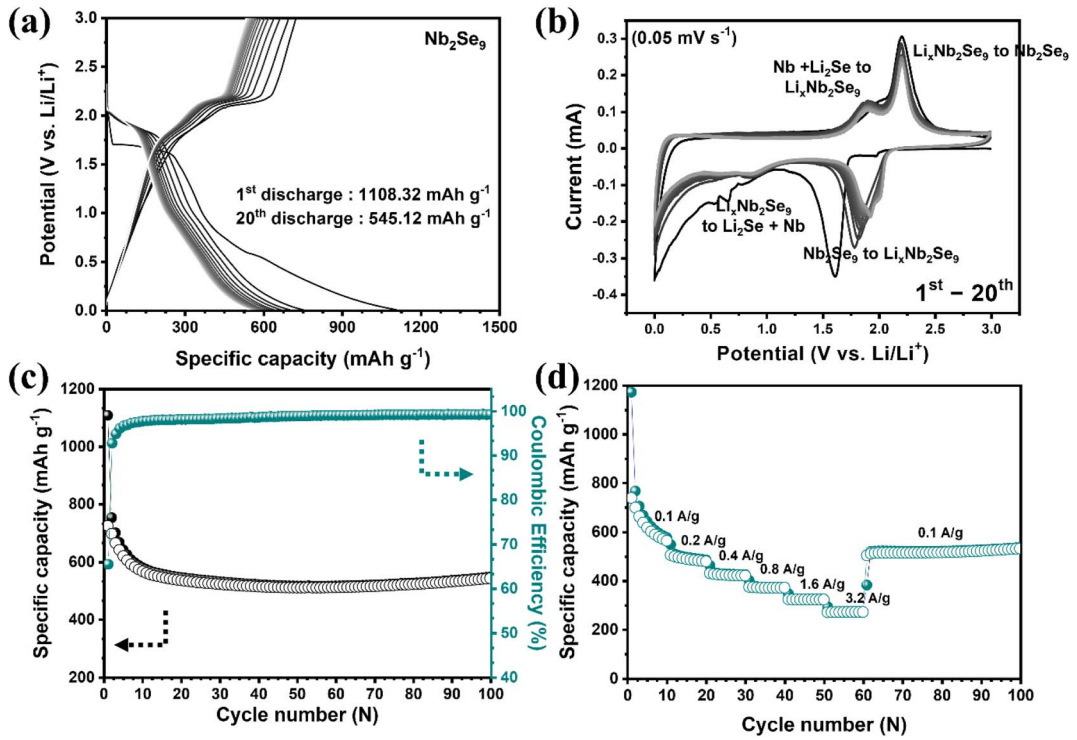

Fig. 2 Electrochemical characterization of Nb_2Se_9. (a) Initial voltage profile. (b) CV curves for initial 20 cycles at a scan rate of 0.05 mV s^{-1}. (c) Cycle performance and coulombic efficiency data of the Nb_2Se_9 electrode at 0.1 A g^{-1}. (d) Rate performance of Nb_2Se_9 at different current rates from 0.1 to 3.2 A g^{-1} in the voltage range of 0.001–3.0 V.

520.2 mA h g^{-1} when the current density was returned to 0.1 A g^{-1} after high-rate cycling (Fig. 2d). After the reaction stabilized and reached the 100th cycle, the electrode showed good capacity retention with a coulombic efficiency of 99.2% and a discharge capacity of 546.5 mA h g^{-1} (Fig. 2c). These results can be ascribed to the unique structural properties of Nb_2Se_9, characterized by its one-dimensional structure and exposed Se atoms, which facilitate the easy migration and reaction of lithium.

CV measurement was conducted at scan rates from 0.1 to 2.0 mV s^{-1} to study the lithium storage behavior (Fig. 3a). The electrochemical response of an active material to different scan rates can be defined as follows:[37]

$$i = av^b, \quad (1)$$

where i represents the obtained current at the peaks, and it exhibits a power-law relationship with the scan rate (v). When a redox reaction is solely controlled by diffusion (or insertion) behavior, the b-value would be 0.5, whereas it would be 1.0 for a surface-controlled capacitive process. The b-value can be calculated by taking logarithm of eqn (1), which would be the slope of the plot between log(i) and log(v). As depicted in Fig. 3b, b-values of peaks 1 and 2 are calculated (0.6222 for peak 1 and 0.6250 for peak 2), and they are close to 0.5, which indicates that the diffusion-controlled insertion process predominates in these peaks. Given that peaks 1 and 2 correspond to the insertion and desertion of lithium ions in Nb_2Se_9 (Fig. 2b), b-values close to 0.5 are reasonable. The surface capacitive contribution was further investigated (Fig. 3c and d). The voltammetric response at a fixed voltage can also be demonstrated using another equation.[38]

$$i(V) = k_1v + k_2v^{1/2} \quad (2)$$

The equation mentioned above is the sum of the current from capacitive effects (k_1v) and diffusion-controlled insertion ($k_2v^{1/2}$). At a scan rate of 1.0 mV s^{-1}, the surface capacitive contribution is 40%, and the capacitive contribution is minimal in the region of peaks 1 and 2, which are near 1.7 V in the cathodic scan and 2.3 V in the anodic scan (Fig. 3c). This finding aligns with the previously mentioned observation, that is, the b-value of peaks 1 and 2 are close to 0.5. Fig. 3d shows the contribution of the surface capacitive effect at various scan rates. As the scan rate increases to 2.0 mV s^{-1}, the contribution of the surface capacitive effect does not surpass 45% of the total current. Therefore, it can be considered that the lithium storage process in Nb_2Se_9 is primarily a diffusion-controlled process.

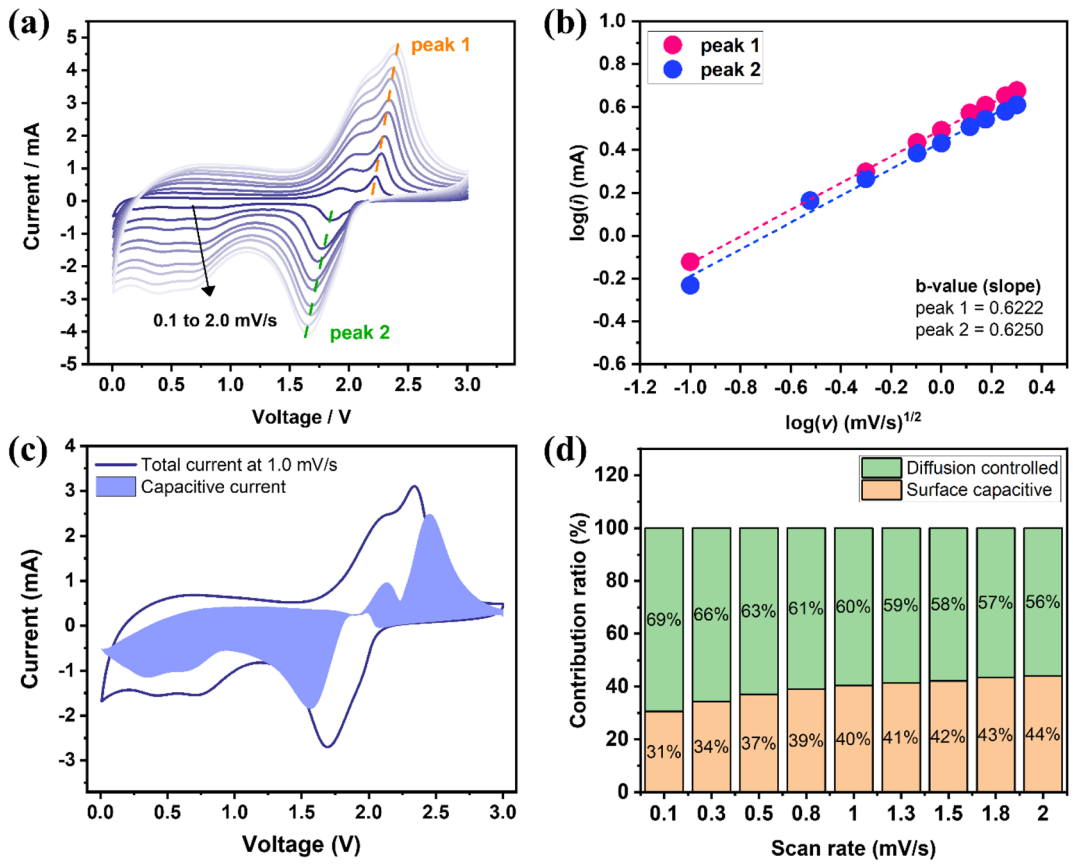

Fig. 3 (a) CV curves of the Nb_2Se_9 electrode at different scan rates from 0.1 to 2.0 mV s^{-1}. (b) log(i)–log(v) plot for peaks 1 and 2. (c) Contribution of the capacitive current at 0.8 mV s^{-1} and (d) contribution ratio of diffusion controlled and surface capacitive processes at different scan rates.

As previously mentioned, the one-dimensional crystal structure of Nb_2Se_9 plays an essential role in its electrochemical performance. However, the previously reported Nb_2Se_9 research was not focused on the mechanistic investigation of lithium storage in detail.[27] Therefore, this study aims to systematically understand the structural effects on lithium storage behavior in Nb_2Se_9 by monitoring its structural dynamics. *In situ* XRD data are collected from the assembled *in situ* coin cell upon the first and second cycles to gain a thorough understanding of the structural behavior of Nb_2Se_9 (Fig. 4). The XRD pattern of pristine Nb_2Se_9 can be indexed to the triclinic phase, which is well-matched to the standard diffraction pattern of Nb_2Se_9 (JCPDS 33-0968). During the first discharge process, the initially observed peaks from Nb_2Se_9 gradually disappeared within the initial 1.5 V plateau region, and no additional peaks were monitored. Therefore, the disruption of the long-range order of a crystal structure can be ascribed to the storage of Li ions through an insertion reaction ($xLi^+ + xe^- + Nb_2Se_9 \rightarrow Li_xNb_2Se_9$) because the formation of Li_2Se was not observed in this voltage range. In addition, the XRD pattern between 14° and 26° related to CNTs disappeared after the plateau reached 0.5 V. This finding is consistent with the cathodic peak position in the first scan of the CNT electrode (Fig. S2b†). The disappearance of the XRD pattern is attributed to the fact that lithiated CNTs become embrittled and shredded due to the large tensile stress in the circumferentially closed carbon layer.[39–41] Besides, after the plateau region around 1.5 V in the first discharge, new peaks emerged near 25.7°, 29.7°, 42.6°, 50.4°, and 52.8°. Such peaks matched well with the standard diffraction patterns of Li_2Se (JCPDS 00-023-0072), and they disappeared entirely after the charging process. The formation of Li_2Se indicates that Li-ion storage occurred through the conversion reaction ($(18 - x)Li^+ + (18 - x)e^- + Li_xNb_2Se_9 \rightarrow 2Nb + 9Li_2Se$). The formation and deformation of Li_2Se were also observed in the second cycle, whereas no signal of Nb metal was observed. This can be explained by the suppression of the conglomeration of metal atoms.[42] In the second cycle, the formation and deformation of Li_2Se were observed just as in the first cycle. Therefore, *in situ* XRD analysis supports the reversible lithium storage process through the conversion reaction.

Ex situ Nb and Se K-edge spectra of Nb_2Se_9, with reference to the spectra obtained during the second cycle, were collected to support the interpretation of *in situ* XRD and obtain insight into the redox reaction occurring in Nb_2Se_9 materials. The detailed structure of one-dimensional Nb_2Se_9 chains is displayed in Fig. 5a. The switching tetra-Se (Se_4) and penta-Se (Se_5) groups are linearly connected along the diagonal direction of <111>.[26,43] The normalized Nb K-edge spectra show a reversible energy

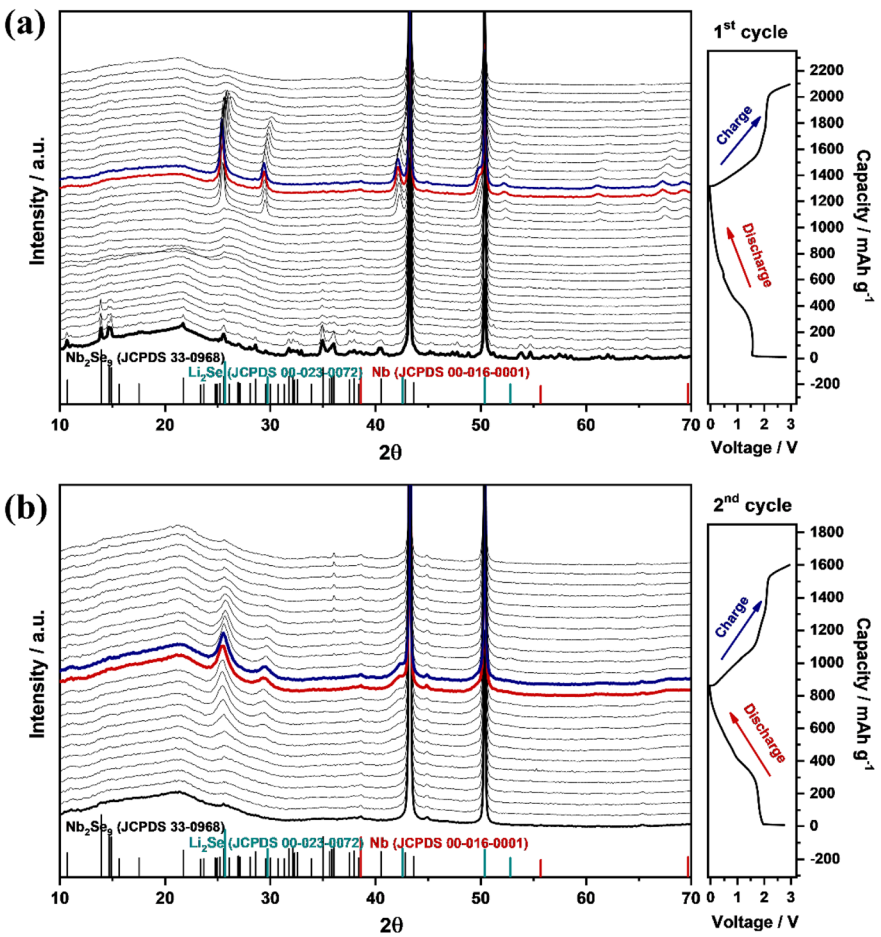

Fig. 4 *In situ* XRD patterns of the Nb_2Se_9 electrode during the (a) first and (b) second cycles along with the voltage profile.

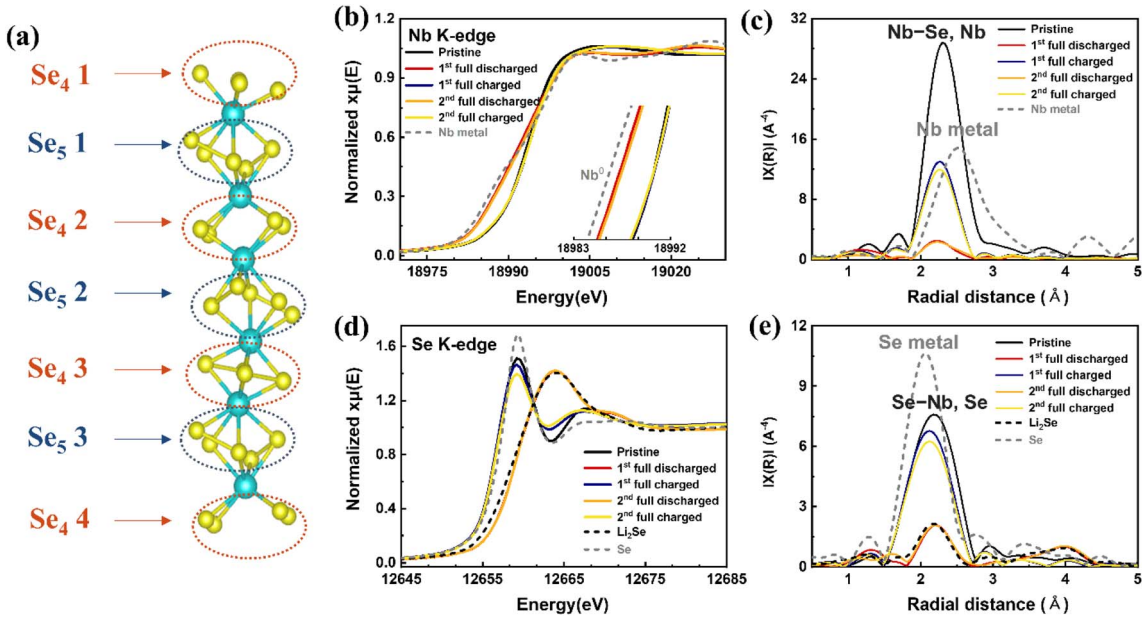

Fig. 5 (a) The atomic arrangement of the one-dimensional Nb_2Se_9 phase with switching tetra-Se (Se_4) and penta-Se (Se_5) groups along linearly connected niobium (Nb) atoms. Normalized (b) Nb and (d) Se K-edge XANES spectra as well as the k^3-weighted Fourier transform magnitude of (c) Nb and (e) Se K-edge EXAFS spectra during the first two cycles.

shift during the two cycles. As shown in X-ray absorption near-edge structure (XANES) spectra and the enlarged main edge spectra in Fig. 5b, the absorption edges shift to lower energies close to the Nb^0 state in the fully discharged state. Then, the absorption edges reversibly shifted toward a high-energy state after the fully charged state until reaching the initial oxidation state of the pristine Nb_2Se_9 electrode. In addition, the similar Nb metal distance of the charged Nb_2Se_9 (2.27 Å) to that of pristine Nb_2Se_9 (2.30 Å) in Fig. 5c supports the formation of the Nb_2Se_9 phase after the fully charged state. The lower intensity of the first shell of charged Nb_2Se_9 than that of pristine Nb_2Se_9 indicates the distorted arrangement of Nb–(Nb, Se), which agrees with the loss of the diffraction pattern of the Nb_2Se_9 phase after the full-charged state (Fig. 4).[44] Even after fully reacting with lithium ions, Nb metal was not detected, although the oxidation state of Nb nearly approached the Nb metallic state (Fig. 5b). As previously mentioned, the growth of metal might have been inhibited by selenide products[45,46] or the formation of the Li_2Se-Nb-Li_2Se phase,[47] which resulted from the conversion reaction.

To investigate the insertion and conversion reaction region during energy storage of Nb_2Se_9, first-principles calculations were conducted. Various Li^+/vacancy configurations of each $Li_xNb_2Se_9$ ($0 \leq x \leq 6$) were generated using CASM. Subsequently, the formation energy for each configuration was calculated and organized into a convex hull diagram (Fig. 6a). In this plot, each ball in the plot represents a different configuration of $Li_xNb_2Se_9$ generated using the CASM software, and the formation energy of the $Li_0Nb_2Se_9$ and $Li_6Nb_2Se_9$ composition was used as a reference. The relative formation energy for the intermediate configuration was derived to determine the stability of the composition.

$$V = -\frac{E[Li_{x_2}Nb_2Se_9] - E[Li_{x_1}Nb_2Se_9] - (x_2 - x_1)E[Li]}{(x_2 - x_1)F},$$

where V represents the mean redox potential within the composition range spanning from x_1 and x_2, and F denotes the Faraday constant. A total of 6 moles of Li ions could be reversibly intercalated and deintercalated in the Nb_2Se_9 structure within the accessible voltage range. Further Li^+ storage based on the conversion reaction was also calculated (Fig. 6b). The theoretical voltage for the conversion-based reaction was derived using the following equation:

$$V = -\frac{(2E[Nb] + 9E[Li_2Se]) - (E[Li_6Nb_2Se_9] - 12E[Li])}{12F}$$

Up to 18 moles of Li ions could be stored in Nb_2Se_9 through the conversion reaction, yielding a theoretical capacity of ~538 mA h g^{-1}. Thus, the subsequent conversion reaction corresponding to ~12 moles Li^+ storage per formula unit of Nb_2Se_9 would occur at an average redox potential of ~1.4 V, resulting in the formation of metallic Nb and Li_2Se. In addition, detailed structural images are presented in Fig. 6c. In the space group of $P\bar{1}$, the Li sites were predicted to be six Wyckoff sites with multiplicity 1 and three Wyckoff sites with multiplicity 2. During Li^+ insertion, each Li^+ was stored between one-dimensional Nb_2Se_9 chains, accompanying the lattice expansion.

The oxidation states of Nb_2Se_9 electrodes were analyzed in detail by examining the first derivatives of the Nb K-edge, as illustrated in Fig. S3,† in light of prior research by Klaes *et al.*[48] The edge positions of Nb were decided by the first inflection points of the spectra. Initially, Nb in pristine Nb_2Se_9 exhibited an oxidation state of +2.88, which was subsequently reduced to

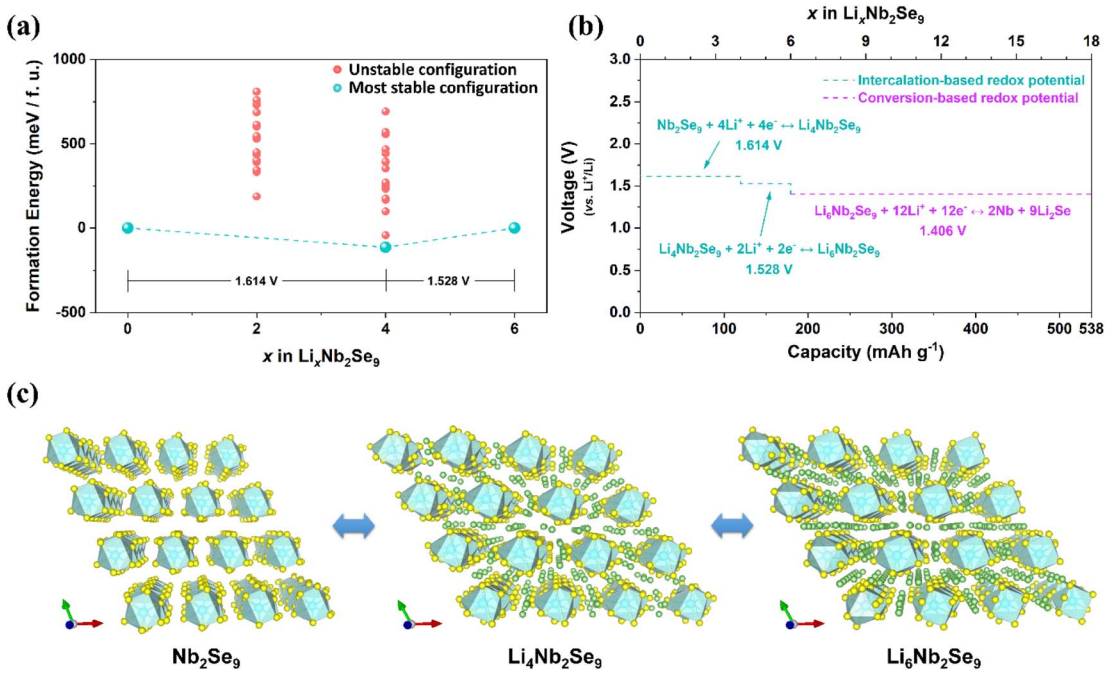

Fig. 6 (a) Formation energy with the calculated theoretical voltage of $Li_xNb_2Se_9$ ($0 \leq x \leq 6$). (b) Theoretical voltage prediction for $Li_xNb_2Se_9$ ($0 \leq x \leq 18$). (c) Calculated $Li_xNb_2Se_9$ ($0 \leq x \leq 6$) structure with Li^+ sites.

+0.13 upon the first full discharge (FD) and eventually restored to +2.95 after full charge (FC), approximating its original state. Similar oxidation states (+0.20 and +2.88) were observed during the second cycle, providing evidence of the reversible redox reaction of Nb during the Li storage process. While Nb undergoes a redox reaction upon cycling, Se also participates in the redox reaction (Fig. 5d). When discharged, the Se K-edge of pristine Nb_2Se_9 shifted from 12 657 to 12 659 eV, which almost overlaps with the absorption edge of the reference Li_2Se spectra after reacting with lithium ions. This finding aligns well with the formation of Li_2Se, as indicated by the *in situ* XRD spectra presented in Fig. 4. The changes observed in the Se K-edge spectra mirrored the reversible trends observed in the V K-edge spectra. It is noteworthy that the Se K-edge shifted to elevated energy after discharge despite Se being reduced during the reaction with lithium ions. This energy shift toward higher energy is due to reduced screening effects by the substantial coulombic interaction between Se^{2-} ions and neighboring Li^+ ions.[49–51] In the Se K-edge EXAFS spectra (Fig. 5e), the formation of Li_2Se after full lithiation and the return to the Nb_2Se_9 phase with a slightly reduced bond length were observed.

The morphological transformation of electrode materials was monitored by SEM to verify the structural sustainability of the Nb_2Se_9 electrode (Fig. S4†). Rod-type Nb_2Se_9 was confirmed in the pristine state (Fig. S4a–c†). Upon cycling, the crystallinity of Nb_2Se_9 was degraded, and it became an amorphous phase, as observed in *in situ* XRD data (Fig. S4d–o†). However, unlike other conversion reactions, where materials lose their initial shapes and form separated transition metal (TM) and Li_2X (X = O or S) phases,[52,53] Nb_2Se_9 maintained its initial rod shape even though it became amorphous during cycling. The superior structural stability can be ascribed to the Se–Se buffer layer and the Se-rich characteristics of the Nb_2Se_9 phase, providing advantages in maintaining structural integrity. As stated by Dang *et al.*,[45,46] homogenously distributed Na_2Se around the TM prevents the coalescing of the TM by forming Na_2Se-TM crystalline interfaces. Moreover, introducing an excess of selenium into the transition metal chalcogenide material leads to excess selenium atoms acting as both a buffer layer and a conductive pathway, effectively mitigating volume expansion.[54] Wang *et al.* also reported that the Se-rich phase exhibits a protective effect, restricting the structural pulverization of the active material by forming the Na_2Se-TM-Na_2Se phase.[55] Therefore, the superior structural stability of Nb_2Se_9 can be attributed to the distinctive 1D vdW structure of Nb_2Se_9 with the Se-rich nature of Nb_2Se_9, which buffers the volume expansion and particle fragmentation.

Conclusions

In summary, one-dimensional van der Waals Nb_2Se_9 was prepared *via* a solid-state reaction and evaluated as a potential LIB anode material. The results show that the Nb_2Se_9 electrode exhibits outstanding electrochemical performance, with a capacity of 542.2 mA h g^{-1} at 0.1 A g^{-1} after 100 cycles and 272.0 mA h g^{-1} at 3.2 A g^{-1}. To investigate the lithium storage behavior of the Nb_2Se_9 electrode, a variety of analysis techniques were employed, including CV, SEM, TEM, *in situ* XRD, and *ex situ* XAS. The results indicate that lithium storage occurs *via* an insertion and conversion reaction that forms Li_2Se at the end of lithiation, as confirmed by DFT calculations. Furthermore, SEM analysis revealed that the electrode exhibited

excellent structural stability during the first two cycles. The one-dimensional structure of Nb_2Se_9 remained intact without collapsing into a wire shape, distinguishing it from conventional conversion reaction materials. The superior electrochemical performance and structural stability of Nb_2Se_9 can be attributed to its Se-rich characteristic, which serves as a buffer layer that relieves volume expansion. Therefore, the unique properties of one-dimensional van der Waals transition metal chalcogenide materials with Se-rich surfaces may offer promising opportunities for designing high-stability and high-energy storage materials.

Author contributions

Woosung Choi: conceptualization, methodology, writing – original draft. Seungbae Oh: conceptualization, methodology, writing – original draft. Sunhyun Hwang: conceptualization, visualization, writing – original draft. Sudong Chae: conceptualization, methodology. Hyunyoung Park: formal analysis, data curation. Wontae Lee: methodology. Chaeheon Woo: data curation. Xue Dong: data curation. Kyung Hwan Choi: data curation. Jungyoon Ahn: data curation. Yeongjin Kim: visualization. Xiaojie Zhang: data curation. Jinsu Kang: data curation. Hyeon-Seok Bang: visualization. Jiho Jeon: visualization. Hyung-Suk Oh: methodology. Jongsoon Kim: supervision. Jae-Young Choi: supervision. Won-Sub Yoon: supervision.

Conflicts of interest

There are no conflicts of interest to declare.

Acknowledgements

This work was supported by a National Research Foundation of Korea (NRF) grant funded by the Korean government (MSIP) (No. NRF-2017R1A4A1015770 and No. NRF-2022R1A2B5B02002624).

References

1 Y. Nishi, *J. Power Sources*, 2001, **100**, 101–106.
2 M. N. Obrovac and V. L. Chevrier, *Chem. Rev.*, 2014, **114**, 11444–11502.
3 X. Zuo, J. Zhu, P. Müller-Buschbaum and Y. J. Cheng, *Nano Energy*, 2017, **31**, 113–143.
4 Y. Jin, B. Zhu, Z. Lu, N. Liu and J. Zhu, *Adv. Energy Mater.*, 2017, **7**, 1700715.
5 C. K. Chan, X. F. Zhang and Y. Cui, *Nano Lett.*, 2008, **8**, 307–309.
6 H. Ying and W. Q. Han, *Adv. Sci.*, 2017, **4**, 1700298.
7 J. H. Um, H. Kim, Y.-H. Cho and W.-S. Yoon, *J. Electrochem. Sci. Technol.*, 2020, **11**, 92–98.
8 J. Yoon, W. Choi, T. Kim, H. Kim, Y. Seok Choi, J. Man Kim and W. S. Yoon, *J. Energy Chem.*, 2020, **53**, 276–284.
9 L. Li, A. R. O. Raji and J. M. Tour, *Adv. Mater.*, 2013, **25**, 6298–6302.
10 Z. S. Wu, W. Ren, L. Wen, L. Gao, J. Zhao, Z. Chen, G. Zhou, F. Li and H. M. Cheng, *ACS Nano*, 2010, **4**, 3187–3194.
11 X. W. Lou, D. Deng, J. Y. Lee, J. Feng and L. A. Archer, *Adv. Mater.*, 2008, **20**, 258–262.
12 Y. M. Lin, P. R. Abel, A. Heller and C. B. Mullins, *J. Phys. Chem. Lett.*, 2011, **2**, 2885–2891.
13 W. Choi, Y. S. Choi, H. Kim, J. Yoon, Y. Kwon, T. Kim, J. H. Ryu, J. H. Lee, W. Lee, J. Huh, J. M. Kim and W. S. Yoon, *Chem. Mater.*, 2021, **33**, 1935–1945.
14 I. Kim, S.-W. Park and D.-W. Kim, *Chem. Eng. J.*, 2019, **375**, 122033.
15 M. T. McDowell, S. W. Lee, W. D. Nix and Y. Cui, *Adv. Mater.*, 2013, **25**, 4966–4985.
16 P. Poizot, S. Laruelle, S. Grugeon, L. Dupont and J. Tarascon, *Nature*, 2000, **407**, 496–499.
17 H. Kim, D. I. Kim and W.-S. Yoon, *J. Electrochem. Sci. Technol.*, 2022, **13**, 32–53.
18 K. Cao, T. Jin, L. Yang and L. Jiao, *Mater. Chem. Front.*, 2017, **1**, 2213–2242.
19 J. Jiang, Y. Li, J. Liu and X. Huang, *Nanoscale*, 2011, **3**, 45–58.
20 S. Oh, S. Chae, B. J. Kim, A. J. Siddiqa, K. H. Choi, W. S. Jang, K. H. Lee, H. Y. Kim, D. K. Lee, Y. M. Kim, H. K. Yu and J. Y. Choi, *Phys. Status Solidi RRL*, 2018, **12**, 2–7.
21 A. Meerschaut, L. Guémas, R. Berger and J. Rouxel, *Acta Crystallogr., Sect. B: Struct. Crystallogr. Cryst. Chem.*, 1979, **35**, 1747–1750.
22 Q. Wu, Y. Zhang, Y. Xia, Y. Chen, G. Diao, L. Lang and M. Chen, *J. Solid State Chem.*, 2023, **321**, 123914.
23 K. Omichi, G. Ramos-Sanchez, R. Rao, N. Pierce, G. Chen, P. B. Balbuena and A. R. Harutyunyan, *J. Electrochem. Soc.*, 2015, **162**, A2106–A2115.
24 X. D. Huang, X. F. Gan, F. Zhang, Q. A. Huang and J. Z. Yang, *Electrochim. Acta*, 2018, **268**, 241–247.
25 D. W. Murphy, F. A. Trumbore and J. N. Carides, *J. Electrochem. Soc.*, 1977, **124**, 325–329.
26 F. O. T. Agyapong-Fordjour, S. Oh, J. Lee, S. Chae, K. H. Choi, S. H. Choi, S. Boandoh, W. Yang, J. Huh, K. K. Kim and J. Y. Choi, *ACS Appl. Energy Mater.*, 2019, **2**, 5785–5792.
27 X. Wu, B. Wu, H. Wang, Q. Zhuang, Z. Xiong, H. Yi, P. Xu, G. Shi, Y. Guo and B. Wang, *Energy Fuels*, 2021, **35**, 11563–11571.
28 R. B. V. D. B. H. Toby, *J. Appl. Crystallogr.*, 2013, **46**, 544–549.
29 G. Kresse and J. Furthmüller, *Comput. Mater. Sci.*, 1996, **6**, 15–50.
30 P. E. Blöchl, *Phys. Rev. B: Condens. Matter Mater. Phys.*, 1994, **50**, 17953–17979.
31 J. P. Perdew, K. Burke and M. Ernzerhof, *Phys. Rev. Lett.*, 1996, **77**, 3865–3868.
32 A. Van der Ven, J. C. Thomas, Q. Xu and J. Bhattacharya, *Math. Comput. Simul.*, 2010, **80**, 1393–1410.
33 J. Lee, B. J. Kim, Y. K. Chung, W. G. Lee, I. J. Choi, S. Chae, S. Oh, J. M. Kim, J. Y. Choi and J. Huh, *J. Raman Spectrosc.*, 2020, **51**, 1100–1107.
34 C. Peng, H. Lyu, L. Wu, T. Xiong, F. Xiong, Z. Liu, Q. An and L. Mai, *ACS Appl. Mater. Interfaces*, 2018, **10**, 36988–36995.

35 J. Zhang, C. Du, J. Zhao, H. Ren, Q. Liang, Y. Zheng, S. Madhavi, X. Wang, J. Zhu and Q. Yan, *ACS Appl. Mater. Interfaces*, 2018, **10**, 37773–37778.
36 E. Hitz, J. Wan, A. Patel, Y. Xu, L. Meshi, J. Dai, Y. Chen, A. Lu, A. V. Davydov and L. Hu, *ACS Appl. Mater. Interfaces*, 2016, **8**, 11390–11395.
37 H. Lindström, S. Södergren, A. Solbrand, H. Rensmo, J. Hjelm, A. Hagfeldt and S.-E. Lindquist, *J. Phys. Chem. B*, 1997, **101**, 7717–7722.
38 A. J. Bard, L. R. Faulkner and H. S. White, *Electrochemical Methods: Fundamentals and Applications*, John Wiley & Sons, 2022.
39 X. H. Liu, J. W. Wang, Y. Liu, H. Zheng, A. Kushima, S. Huang, T. Zhu, S. X. Mao, J. Li, S. Zhang, W. Lu, J. M. Tour and J. Y. Huang, *Carbon*, 2012, **50**, 3836–3844.
40 Y. Liu, H. Zheng, X. H. Liu, S. Huang, T. Zhu, J. Wang and A. Kushima, *ACS Nano*, 2011, **5**, 7245–7253.
41 N. Li and D. Su, *Carbon Energy*, 2019, **1**, 200–218.
42 H. Kim, W. Ih Choi, Y. Jang, M. Balasubramanian, W. Lee, G. Ok Park, S. Bin Park, J. Yoo, J. Seok Hong, Y.-S. Choi, H. Sug Lee, I. Tae Bae, J. Man Kim and W.-S. Yoon, *ACS Nano*, 2018, **12**, 2909–2921.
43 W. G. Lee, S. Chae, Y. K. Chung, S. Oh, J. Y. Choi and J. Huh, *Phys. Status Solidi RRL*, 2019, **13**, 2–7.
44 D. J. Sprouster and M. C. Ridgway, *Appl. Sci.*, 2012, **2**, 396–442.
45 H. X. Dang, M. L. Meyerson, A. Heller and C. B. Mullins, *RSC Adv.*, 2015, **5**, 82012–82017.
46 H. X. Dang, K. C. Klavetter, M. L. Meyerson, A. Heller and C. B. Mullins, *J. Mater. Chem. A*, 2015, **3**, 13500–13506.
47 X. H. Liu, J. W. Wang, Y. Liu, H. Zheng, A. Kushima, S. Huang, T. Zhu, S. X. Mao, J. Li, S. Zhang, W. Lu, J. M. Tour and J. Y. Huang, *Carbon*, 2012, **50**, 3836–3844.
48 J. Klaes, P. Rothweiler, B. Bornmann, R. Wagner and D. Lützenkirchen-Hecht, *J. Synchrotron Radiat.*, 2021, **28**, 266–277.
49 Y. Cui, A. Abouimrane, C. J. Sun, Y. Ren and K. Amine, *Chem. Commun.*, 2014, **50**, 5576–5579.
50 Y. Cui, A. Abouimrane, J. Lu, T. Bolin, Y. Ren, W. Weng, C. Sun, V. A. Maroni, S. M. Heald and K. Amine, *J. Am. Chem. Soc.*, 2013, **135**, 8047–8056.
51 R. Alonso Mori, E. Paris, G. Giuli, S. G. Eeckhout, M. Kavčič, M. Žitnik, K. Bučar, L. G. M. Pettersson and P. Glatzel, *Anal. Chem.*, 2009, **81**, 6516–6525.
52 Q. Su, S. Wang, M. Feng, G. Du and B. Xu, *Sci. Rep.*, 2017, **7**, 1–10.
53 J. Li, S. Hwang, F. Guo, S. Li, Z. Chen, R. Kou, K. Sun, C. J. Sun, H. Gan, A. Yu, E. A. Stach, H. Zhou and D. Su, *Nat. Commun.*, 2019, **10**, 2224.
54 Y. Huang, Z. Wang, Y. Jiang, S. Li, Z. Li, H. Zhang, F. Wu, M. Xie, L. Li and R. Chen, *Nano Energy*, 2018, **53**, 524–535.
55 X. Wang, Z. Yang, C. Wang, D. Chen, R. Li, X. Zhang, J. Chen and M. Xue, *J. Power Sources*, 2017, **369**, 138–145.